

Electronic polarization effects in the photodissociation of Cl₂

E. K. Campbell, A. B. Alekseyev, G. G. Balint-Kurti, M. Brouard, Alex Brown et al.

Citation: *J. Chem. Phys.* **136**, 164311 (2012); doi: 10.1063/1.4704830

View online: <http://dx.doi.org/10.1063/1.4704830>

View Table of Contents: <http://jcp.aip.org/resource/1/JCPSA6/v136/i16>

Published by the [American Institute of Physics](#).

Additional information on *J. Chem. Phys.*


Journal Homepage: <http://jcp.aip.org/>

Journal Information: http://jcp.aip.org/about/about_the_journal

Top downloads: http://jcp.aip.org/features/most_downloaded

Information for Authors: <http://jcp.aip.org/authors>

ADVERTISEMENT



AIPAdvances

Special Topic Section:
PHYSICS OF CANCER

Why cancer? Why physics? [View Articles Now](#)

Electronic polarization effects in the photodissociation of Cl₂

E. K. Campbell,¹ A. B. Alekseyev,² G. G. Balint-Kurti,³ M. Brouard,^{1,a)} Alex Brown,⁴
R. J. Buenker,² R. Cireasa,¹ A. J. Gilchrist,¹ A. J. Johnsen,¹ D. B. Kokh,² S. Lucas,¹
G. A. D. Ritchie,¹ T. R. Sharples,¹ and B. Winter¹

¹The Department of Chemistry, University of Oxford, The Physical and Theoretical Chemistry Laboratory,
South Parks Road, Oxford OX1 3QZ, United Kingdom

²Fachbereich C-Mathematik und Naturwissenschaften, Bergische Universität,
Gaussstr. 20, D-42119 Wuppertal, Germany

³Centre for Computational Chemistry, School of Chemistry, University of Bristol,
Bristol BS8 1TS, United Kingdom

⁴Department of Chemistry, University of Alberta, Edmonton, Alberta T6G 2G2, Canada

(Received 26 January 2012; accepted 30 March 2012; published online 27 April 2012)

Velocity mapped ion imaging and resonantly enhanced multiphoton ionization time-of-flight methods have been used to investigate the photodissociation dynamics of the diatomic molecule Cl₂ following excitation to the first UV absorption band. The experimental results presented here are compared with high level time dependent wavepacket calculations performed on a set of *ab initio* potential energy curves [D. B. Kokh, A. B. Alekseyev, and R. J. Buenker, J. Chem. Phys. **120**, 11549 (2004)]. The theoretical calculations provide the first determination of all dynamical information regarding the dissociation of a system of this complexity, including angular momentum polarization. Both low rank $K = 1, 2$ and high rank $K = 3$ electronic polarization are predicted to be important for dissociation into both asymptotic product channels and, in general, good agreement is found between the recent theory and the measurements made here, which include the first experimental determination of high rank $K = 3$ orientation. © 2012 American Institute of Physics. [<http://dx.doi.org/10.1063/1.4704830>]

I. INTRODUCTION

The photodissociation of Cl₂ has been investigated in considerable detail in the past, with experimental studies dating back to the 1960s.^{1,2} While early studies focussed on the spatial anisotropy parameter and the branching ratio between the two important asymptotic product channels (Cl(²P_{3/2}) + Cl(²P_{3/2}) and Cl(²P_{3/2}) + Cl(²P_{1/2})),^{3–6} the electronic angular momentum distributions of both the ground Cl(²P_{3/2}) (labelled herewith Cl) and excited Cl(²P_{1/2}) (labelled Cl*) state atomic photofragments have been probed in later work,^{7–15} giving rise to a detailed description of the bond breaking process. In addition to the experimental work, there have been numerous theoretical studies into both the electronic structure and dissociation dynamics of this diatomic molecule.^{16–21} For a more detailed account of previous experimental and theoretical work on the photodissociation of Cl₂, the reader is referred to the accompanying paper.²² Despite the wide ranging literature, only very recently has there been a fully quantum mechanical treatment of the photodissociation of Cl₂. In the accompanying paper,²² time-dependent wavepacket calculations are presented, similar to those used by Balint-Kurti and co-workers to investigate the photolysis of the hydrogen halides.^{23–27} These calculations, which implicitly included non-adiabatic effects and were performed on a set of *ab initio* potential energy curves,²⁰ have allowed the extraction of all dynamical information regarding the dissociation.²²

In the present work, the photodissociation of Cl₂ has been investigated experimentally over a wide range of

photolysis wavelengths across the absorption band allowing the determination of both the low rank and high rank polarization parameters for dissociation into both of the accessed asymptotic product channels, (Cl + Cl) and (Cl + Cl*). The experiments employed both velocity map²⁸ ion imaging,²⁹ and resonantly enhanced multiphoton ionization (REMPI) time-of-flight (TOF) techniques. The new experimental data are used to provide a detailed test of the quantum dynamical calculations presented in the accompanying paper,²² and of the potential energy curves and coupling matrix elements on which they rely.²⁰ Comparisons of the calculations with both the new and previous experimental results, including the absorption cross-section, the wavelength dependent branching ratio, translational anisotropy parameters, β , and angular momentum polarization parameters, are also presented.

The paper is organized as follows. Sec. II describes the experimental procedures employed, and Sec. III presents and discusses the experimental results in light of previous work and in comparison with those calculated using the quantum mechanical wavepacket methods described in the accompanying paper.²² The paper finishes with a short section outlining our principal conclusions, and suggesting possible future areas of research.

II. EXPERIMENTAL AND ANALYSIS PROCEDURES

A. Ion imaging procedures

1. Ion imaging experiments

The experiments were carried out using a standard velocity map²⁸ ion imaging²⁹ apparatus, which has been described

^{a)}Electronic mail: mark.brouard@chem.ox.ac.uk.

in detail in previous publications (see, for example, Ref. 30). 0.5% Cl₂ was seeded in He at a backing pressure of 2 bar and expanded through a pulsed nozzle (Jordan valve) with a 0.5 mm diameter orifice. The resulting molecular beam was collimated by a 1 mm skimmer. The pulsed, skimmed molecular beam was passed through a 2 mm hole in the repeller plate of the velocity map ion optics assembly and was crossed by two counter propagating laser beams 5 cm away from the nozzle exit. The 376 – 470 nm pump/photodissociation radiation was provided by a Lambda Physik LPD3000 dye laser pumped with the third harmonic of a Nd:YAG laser. The 355 nm photolysis radiation was provided by the third harmonic of a Nd:YAG laser. The probe laser radiation was provided by the second harmonic of a Sirah Cobra Stretch dye laser pumped using the third harmonic of a Nd:YAG laser. The linearly polarized pump laser radiation was passed through a Rochon polarizer and focussed into the region between the repeller and extractor plates using a 30 cm focal length lens. Circularly polarized pump radiation was generated by passing linearly polarized laser radiation through a Fresnel rhomb with the polarization axis at 45° to the principle axis of the rhomb. The probe laser radiation was passed through a photoelastic modulator (PEM-90, Hinds Instruments, Inc.) and focussed using a 30 cm lens. Use of a photoelastic modulator allowed the probe laser to switch between horizontal and vertical polarizations on alternative shots. Furthermore, use of the PEM allowed switching between left (L) and right (R) circular polarizations on alternative laser shots. The time delay between the pump and probe lasers was <10 ns.

The Cl photofragments were ionized using the (2 + 1) REMPI transitions *via* the ²P_{1/2} and ²D_{5/2} intermediate states at 234.5 and 236.2 nm, respectively. The probe laser power was attenuated so as to avoid saturation of both the 2-photon step of the (2 + 1) REMPI transition and the ion counting algorithm. During image acquisition, the probe laser was scanned over the Doppler profile of the REMPI transition to obtain equal detection sensitivities for all product velocities.

The ions were velocity mapped onto an imaging detector consisting of a pair of 75 mm chevron double microchannel plates coupled to a P47 phosphor screen (Burle). The resulting images on the screen were captured by an intensified charge coupled device camera (Photonic Science), electronically gated to the time-of-flight of the ions of interest, and sent to a personal computer for thresholding, event counting, and accumulation. Images were averaged over at least 15 000 laser shots.

To enable the extraction of all polarization information, images were collected in several pump-probe geometries using both REMPI transitions for the Cl atomic products. Labels are assigned to the different pump-probe geometries in order to describe the polarization of light in the time-of-flight frame (see, for example, Ref. 30). The first letter (or number) of each label corresponds to the pump and the second to the probe laser polarization. V and H refer to geometries in which the electric vector of the light lies perpendicular or parallel to the image plane, respectively. (Note that in the time-of-flight frame, the molecular beam direction lies perpendicular to the image plane.) In addition to H and V geometries, images were also collected with the (linearly polarized) electric vector of

the pump laser at ±45° to the time-of-flight axis, as well as with both left (L) and right (R) circularly polarized photolysis *and* probe radiation. The use of both a large number of laser polarization geometries and two REMPI transitions allowed for the determination of the *K* = 1 – 3 moments of the electronic angular momentum distribution for the Cl atomic photofragments.

2. Ion image analysis

Extraction of data from the experimental ion images was performed following the Fourier moment analysis procedure,³¹ as described in detail previously.^{30,32–34} This allows determination of the speed distribution, the speed dependence of the spatial anisotropy parameter, and the speed dependence of the laboratory frame polarization parameters from a set of velocity map ion images. In summary, the starting point for the analysis is the expression of the experimental ion image as a Fourier series in the angular coordinate, ϕ :

$$\mathcal{I}(r, \phi) = c_0(r) + 2 \sum_{n>0} c_n(r) \cos n\phi + c'_n(r) \sin n\phi. \quad (1)$$

Fourier moments (coefficients) of the experimental image are then generated by integrating over the angular coordinate, ϕ , at each value of r

$$c_n(r) = \int_0^{2\pi} \mathcal{I}(r, \phi) \cos(n\phi) r d\phi, \\ c'_n(r) = \int_0^{2\pi} \mathcal{I}(r, \phi) \sin(n\phi) r d\phi. \quad (2)$$

The intensity of a velocity map ion image can be written theoretically in terms of the angular momentum state multipole moments,⁹ $\rho_{KQ}(r, \phi)$, as shown by Suits and coworkers,^{9,35–37} but adapted for multiple recoil velocities,³⁰

$$I(r, \phi : v) = Z \sum_{KQ} \tilde{P}_K \rho_{KQ}(r, \phi : v) C_{KQ}^*(\theta_p, \phi_p), \quad (3)$$

where Z is a normalization constant, \tilde{P}_K are linestrength factors,³⁸ and the angles in the modified spherical harmonic (θ_p, ϕ_p) define the probe laser polarization in the time-of-flight frame. By integrating over the velocity component along the time-of-flight axis, the simulated image intensity can also be cast as a Fourier series in ϕ ,

$$I(r, \phi) = \text{Re}[C_0(r)] + \sum_{n>0} \text{Re}[C_{n+}(r)] \cos n\phi \\ - \text{Im}[C'_{n-}(r)] i \sin n\phi. \quad (4)$$

The simulated Fourier moments, $C_{n\pm}(r)$, are given by

$$C_{n\pm}(r) = \sum_s \sum_{K,q,q'} a_K(q, q'; s) G(K, q, q', n\pm; r), \quad (5)$$

where the (geometry specific) $G(K, q, q', n\pm; r)$ represent a set of basis functions for the simulated ion images.³⁰ For their explicit form, the reader is referred to Ref. 30. The simulated Fourier moments are seen to depend on dynamical functions, $a_K(q, q'; s)$, which are defined below. Note that the basis

functions are fully calculable provided that the linestrength (\bar{P}_K) of the REMPI transition is known.

It is helpful to introduce the dynamical functions, $f'_K(q, q'; v)$,³⁹ which contain all of the electronic angular momentum polarization information of interest.^{9,39} In the present analysis procedure, these are renormalized³⁰ and have the following explicit form:

$$f'_K(q, q'; v) = \frac{f_K(q, q'; v)}{\langle f_0(0, 0; v) \rangle + 2\langle f_0(1, 1; v) \rangle}, \quad (6)$$

where $\langle f_K(q, q'; v) \rangle$ represents integrating the dynamical function over the recoil speed. The dynamical functions are determined by fitting the experimental Fourier moments (Eq. (2)) to the simulated moments (Eq. (5)). To this end, the speed dependence of the dynamical functions is accounted for by expressing them as a linear combination of Gaussian functions centred at a series of equally spaced speeds, v_s :

$$f'_K(q, q'; v) = N \sum_{s=0}^{s_{\max}} a_K(q, q'; s) \exp^{-\sigma(v_s - v)^2}, \quad (7)$$

where the factor N is a normalization constant, $a_K(q, q'; s)$ are the Gaussian specific polarization parameters, and σ defines the width and v_s defines the center of each Gaussian.

In order to reduce the number of fitting coefficients, the speed dependence of the higher order ($n > 0$) $a_K(q, q'; s)$ parameters was expressed as an expansion in Legendre polynomials, multiplied by the speed distribution, $a_0(s)$:

$$a_K(q, q'; s) = a_0(s) \sum_{l=0}^{n_{\text{leg}}} a'_K(q, q'; l) P_l(x_s), \quad (8)$$

where

$$x_s = 2 \frac{s - 1}{s_{\max} - 1} - 1 \quad (9)$$

is constrained between the physically allowed limits of ± 1 .

The quality of the fit (χ^2) was determined by direct comparison of the experimentally measured and simulated Fourier moments (of equivalent order, n). A pool of the fitted $a_K(q, q'; s)$ parameters was randomly generated and then selected using a genetic algorithm routine. The best fit to the experimental data was then determined by the lowest value of χ^2 . A Monte Carlo based procedure (see, for example, Ref. 31) was used to determine the errors on the fitted coefficients and angular distribution.

A further complication exists for the detection of polarized Cl photofragments in that coupling of the electronic angular momentum with the unpolarized nuclear spin reduces the polarization intrinsic to the photodissociation process. This hyperfine depolarization effect, however, can be quantified by the equation⁴⁰

$$g^{(K)} = \sum_F \frac{(2F + 1)^2}{(2I + 1)} \left\{ \begin{matrix} F & F & K \\ J & J & I \end{matrix} \right\}^2, \quad (10)$$

where K describes the photofragment rank, I is the nuclear spin, and F is the total (electronic plus nuclear spin) angular momentum. Specifically for $\text{Cl}(^2\text{P}_{3/2})$, Eq. (10) gives $g^{(1)} = 0.5$, $g^{(2)} = 0.27$, and $g^{(3)} = 0.2$. The reduction coefficients,

$g^{(K)}$, are absorbed into the linestrength factors, \bar{P}_K , to account for the hyperfine depolarization in the data analysis.

B. REMPI TOF procedures

1. REMPI TOF experiments

The REMPI TOF experiment follows the general procedure outlined previously.⁴¹ An effusive molecular beam of 5% Cl_2 diluted in helium at backing pressures between 200 and 250 Torr was introduced into the vacuum chamber *via* a pulsed valve (general valve) and crossed at right angles by counter-propagating photolysis and probe beams within the source region of a modified Wiley-McLaren mass spectrometer. The backing pressures and concentrations employed have previously been found to be sufficient to avoid the formation of clusters in molecular beam experiments,^{13–15} and changing this backing pressure had no effect on the shapes of the signals measured in these experiments. The conditions are such that the rotational temperature of the beam was 140 ± 10 K (determined from previous measurements taken on NO under identical conditions). The frequency doubled output of a Nd-YAG pumped dye laser system (LAS – Spectra Physics) operating with DCM laser dye in methanol provided the photolysis light in the wavelength range 320–330 nm. Following photolysis, the Cl^* fragments were ionized *via* the $3s^2 3p^4 4p^1 (^2\text{P}_{3/2}) \leftarrow \leftarrow 3s^2 3p^5 (^2\text{P}_{1/2}) (2 + 1)$ transition at 236.527 nm by the frequency doubled output of a second Nd-YAG pumped dye laser system (Sirah–Continuum) operated with C480 laser dye in ethanol. Similarly, the Cl photofragments were probed *via* the $3s^2 3p^4 4p^1 (^2\text{S}_{1/2}) \leftarrow \leftarrow 3s^2 3p^5 (^2\text{P}_{3/2}) (2 + 1)$ transition at 234.640 nm.⁴² The resulting ions were subsequently focussed onto a set of microchannel plates, where the distribution of their arrival times was recorded by a digital oscilloscope (LeCroy 9350A). Extraction of polarization information involved holding one laser beam at a single polarization geometry using a Glan-Taylor prism, while the other beam polarization was switched between two linear geometries, or left and right circularly polarized light using a photoelastic modulator (PEM-90, Hinds Instruments Inc.). During the course of a single experimental run, the probe laser was swept over the REMPI transition in steps of 0.0005 nm and profiles were averaged over 100 sweeps. For each of these sets of 100 sweeps, the signals produced by the probe and pump laser alone were recorded and, following power normalization, subtracted from the total signal to yield the true pump-probe signal. The profiles were symmetrized by reflecting down the line centre, base-line corrected, area normalized, and finally simulated in a multi-variable fit, with both experimental parameters and parameters describing the vector correlations of interest as variables, as discussed in Sect. II B 2.

2. REMPI TOF data analysis

The shape of a TOF profile for the case of a single photon dissociation and $(2 + 1)$ REMPI probing may be expressed in terms of the fractional velocity component $x = v_{\text{TOF}}/v$ as⁴³

$$g(x) = g_0 + g_2 P_2(x) + g_4 P_4(x) + g_6 P_6(x), \quad (11)$$

where $P_n(x)$ is the Legendre polynomial of degree n . The g_k coefficients may be expressed in terms of the probe transition sensitivity factors q_k , the bipolar moments,⁴⁴ and the experimental geometry, defined in terms of three angles θ , χ , and ϕ ; θ is the angle between the photolysis electric vector \mathbf{e}_d and the TOF axis \mathbf{k}_{TOF} , χ is the angle between the probe laser electric vector \mathbf{e}_p and \mathbf{e}_d , and ϕ is the angle between the projections of \mathbf{k}_{TOF} and \mathbf{e}_p onto a plane perpendicular to \mathbf{e}_d . In general, the TOF profile shape depends on a large number of vector correlations and we choose pairs of experimental geometries such that the dependence of the difference between them on a single bipolar moment is maximized. Four pairs of geometries, referred to as geometry pairs I–IV, were used in this work and a further *double magic angle* geometry was employed to determine the experimental factors used to model both the temporal width of the probe laser and core extraction. These parameters are determined in a multi-variable least squares fit to the double magic angle profile using a trust – region reflective algorithm available as a built in function in MATLAB.⁴⁵ The measured bipolar moments were subsequently transformed into the recoil frame polarization parameters.⁴⁶

The orientation of the Cl^* fragment is measured using circularly polarized probe light, while the alignment of the Cl fragment is measured using linearly polarized light. In the former case, since $J = 1/2$, only moments with $k \leq 1$ are non-zero. Therefore, for photolysis with linearly polarized light, only β and the $\text{Im}[a_1^{(1)}(\parallel, \perp)]$ parameter describing the orientation of \mathbf{J} are non-zero.⁴⁶ These may be measured from the difference between profiles recorded in two geometry pairs I and IV. In geometry pair I, the probe laser polarization is held at the magic angle to the TOF axis and the photolysis laser polarization is switched from horizontal (H) (i.e., parallel to the TOF axis) to vertical (V) (i.e., perpendicular to the TOF axis), while in geometry pair IV, the photolysis laser is held at 45° to the TOF axis and the probe laser is switched from left (L) to right (R) circular polarization, respectively. The difference profiles for these two geometry pairs are

$$\Delta g_{\text{I}}(x) = \frac{3}{2}\beta P_2(x), \quad (12)$$

$$\Delta g_{\text{IV}}(x) = \sqrt{2}q_1 \text{Im}[a_1^{(1)}(\parallel, \perp)] P_2(x). \quad (13)$$

Note that the probe transition sensitivity factor, q_1 , in Eq. (13) includes a factor $g^{(1)}$ to account for depolarization of the Cl^* electronic angular momentum due to hyperfine coupling.⁴⁰

The alignment of the $\text{Cl}(^2\text{P}_{3/2})$ fragments is measured in geometry pairs II (photolysis laser is H and the probe laser is switched between H and V) and III (photolysis laser is held at the magic angle and the probe laser is switched between H and V). Since $J = 3/2$ for these fragments, only rank $k \leq 3$ parameters⁴⁶ are non-zero, and so for probing with linearly polarized light, profiles depend on the β parameter and the $a_0^{(2)}(\parallel)$, $a_0^{(2)}(\perp)$, $a_2^{(2)}(\perp)$, and $\text{Re}[a_1^{(2)}(\parallel, \perp)]$ polarization parameters.⁴⁶ In these experiments over the wavelength range 320–350 nm, however, the β parameter is found to be very close to -1 , indicating that the dissociation occurs *via* a perpendicular transition (see Sec. III). In order to simplify the analysis, a pure perpendicular transition is assumed, such that

only the parameters $a_0^{(2)}(\perp)$ and $a_2^{(2)}(\perp)$ are non-zero. Rakitzis *et al.*⁴⁷ discuss how the bipolar moments of Dixon⁴⁴ may be related to the recoil frame polarization parameters and how these expressions may be used to derive relationships between TOF profile line shapes and the polarization parameters. For a pure perpendicular transition, the $\beta_0^{(2)}(0, 2)$ bipolar moment may be written as

$$\beta_0^{(2)}(0, 2) = -\frac{1}{4}a_0^{(2)}(\perp) + \frac{\sqrt{6}}{2}a_2^{(2)}(\perp), \quad (14)$$

and so a determination of this moment from the ratio of areas in geometry pair II yields a relationship between the two polarization parameters. These are then determined in a least squares multi-variable fit to the difference profile obtained in geometry pair III

$$\begin{aligned} \Delta g_{\text{III}}(x) = & q_2 \left(\frac{1}{10}a_0^{(2)}(\perp) - \frac{\sqrt{6}}{5}a_2^{(2)}(\perp) \right) \\ & + q_2 \left(\frac{19}{14}a_0^{(2)}(\perp) - \frac{\sqrt{6}}{5}a_2^{(2)}(\perp) \right) P_2(x) \\ & + q_2 \left(\frac{3}{70}a_0^{(2)}(\perp) - \frac{\sqrt{6}}{70}a_2^{(2)}(\perp) \right) P_4(x) \end{aligned} \quad (15)$$

in which the two polarization parameters are allowed to vary with respect to each other in accordance with Eq. (14), where the value of $\beta_0^{(2)}(0, 2)$ is allowed to vary within the error on its measurement.

As noted above, the determination of the polarization parameters first requires knowledge of the temporal width of the probe laser and the core extraction parameters. These are again determined from a least squares multi-variable fit to profiles measured in the double magic angle geometry and are then allowed to vary within their uncertainties in subsequent fits to determine the translational anisotropy and angular momentum polarization. In all cases, the uncertainties were estimated using the technique of Monte Carlo sampling. 1000 synthetic data sets were generated for each piece of data presented, sufficient to ensure convergence of the returned errors to within the precision with which they are reported.

III. RESULTS AND DISCUSSION

A. Ion images and fits

The ion images presented here were obtained following the photodissociation of Cl_2 at eight wavelengths between 355 nm and 470 nm. A selection of ion images collected in a HH pump-probe geometry is shown in Fig. 1(a). At the specific wavelengths studied here longer than 355 nm, the Cl ion images contain contributions from both the $\text{Cl} + \text{Cl}$ and $\text{Cl} + \text{Cl}^*$ product channels. Additional signal arising from the photodissociation of vibrationally excited parent molecules is also observed, which is discussed in a forthcoming publication.⁴⁸ Differences observed between ion images collected with the same pump laser polarization, but different probe laser polarization, indicate non-zero electronic polarization of the Cl photofragments. For example, the isotropic VV and anisotropic VH ion images recorded following photodissociation at 355 nm, as shown in Fig. 1(b), indicate electronic alignment in the $\text{Cl} + \text{Cl}$ product channel. Furthermore, orientation of the Cl fragments can also be observed by

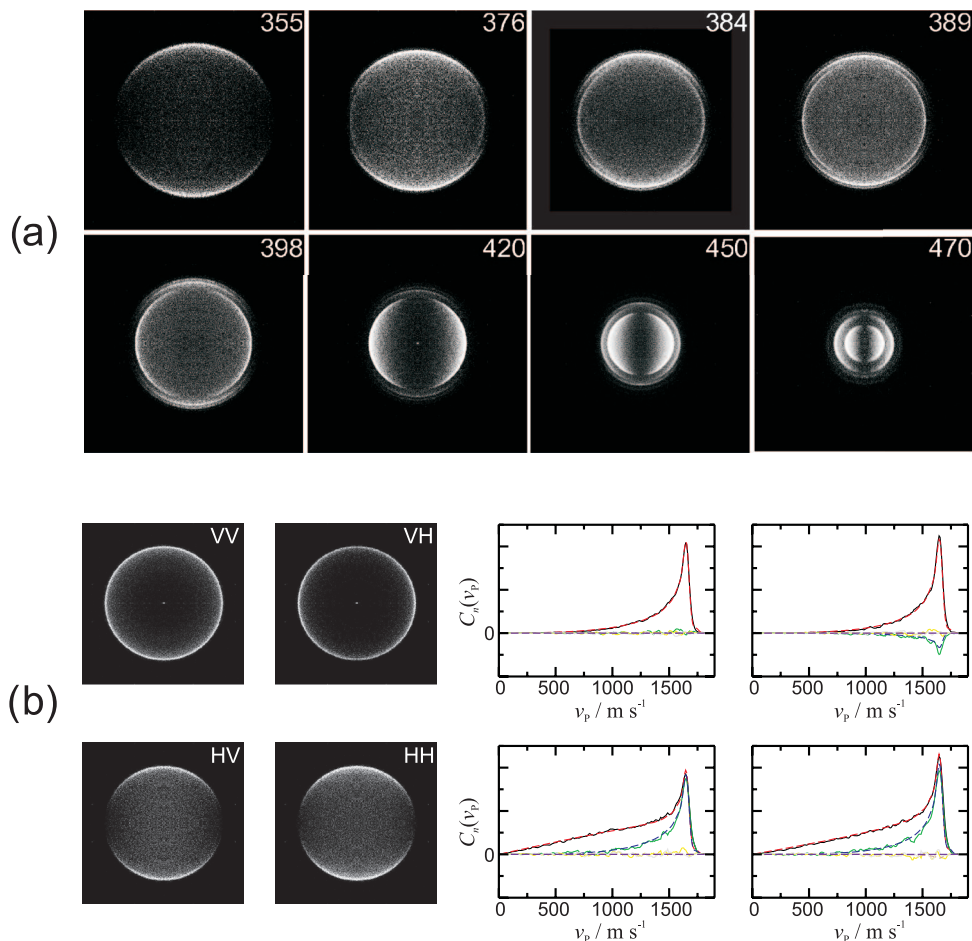


FIG. 1. (a) Selection of Cl ion images following photodissociation of Cl₂ at a range of wavelengths. The ion images were recorded in the HH pump-probe geometry, and used the $^2P_{1/2} \leftarrow ^2P_{3/2}$ REMPI transition at 236.2 nm. (b) Ion images for different pump-probe geometries (left), Fourier moments (—) and fits (---) (right) to the Cl data obtained for photolysis at 355 nm, with the $n = 0, 2$, and 4 experimental Fourier moments shown as red, green, and yellow continuous lines. Images were recorded using the $^2P_{1/2} \leftarrow ^2P_{3/2}$ REMPI transition at 236.2 nm.

inspecting images recorded using circularly polarized light, as illustrated in Fig. 2.

The speed distributions, $P(v)$, returned from the fits to the Cl Fourier moments are shown in Fig. 3. The distributions illustrate the contributions from both the ground and excited state product channel, in addition to the photodissociation of vibrationally excited Cl₂($v = 1$).⁴⁸

B. REMPI TOF data

REMPI TOF data were taken over the wavelength range 320–350 nm and an example of symmetrized profiles and simulated fits for the $^{35}\text{Cl}^*$ and $^{37}\text{Cl}^*$ fragments are shown in Figs. 4(a) and 4(b), respectively, for photolysis at 320 nm at the double magic angle geometry. A significant degree of core extraction is evident in the pronounced dip in the centre of the profile displayed in Figs. 4(a) and 4(b), but the good agreement between the data and the simulations gives confidence that the fitting routine successfully accounts for this effect. For comparison, Fig. 4(c) shows the difference profiles and best fit for photolysis at 320 nm using geometry pair I, $\Delta g_1(x)$. In this case, the shape of the (difference) profile allows the translational anisotropy to be determined. A final example of

the form of data obtained is also shown in Fig. 4(d), where we show the difference profile and best fits to the difference profile obtained in geometry pair IV, $\Delta g_{IV}(x)$, for photolysis at 330 nm and detection of $^{35}\text{Cl}^*$; these data clearly show that the electronic angular momentum of the nascent Cl* product is oriented.

C. Branching ratios

The Cl*/Cl branching ratio (or, more precisely, the branching fraction) has been defined previously as²⁰

$$\text{Cl}^*/\text{Cl} = \frac{\sigma_{\text{Cl}^*}}{\sigma_{\text{Cl}^*} + 2\sigma_{\text{Cl}}}, \quad (16)$$

where σ_{Cl^*} and σ_{Cl} represent the sum of the partial cross-sections for the ground and excited state product channels, respectively. The factor of two in the denominator arises since two Cl($^2P_{3/2}$) atoms are formed in the ground state channel, whereas only one is formed in the excited state channel. The experimental data, as determined from the intensities of the different features seen in the ion images, are shown in Fig. 5 along with the present theoretical results. Agreement between experiment and theory is extremely good, and is consistent with the previous experimental data from Samartzis *et al.*¹³

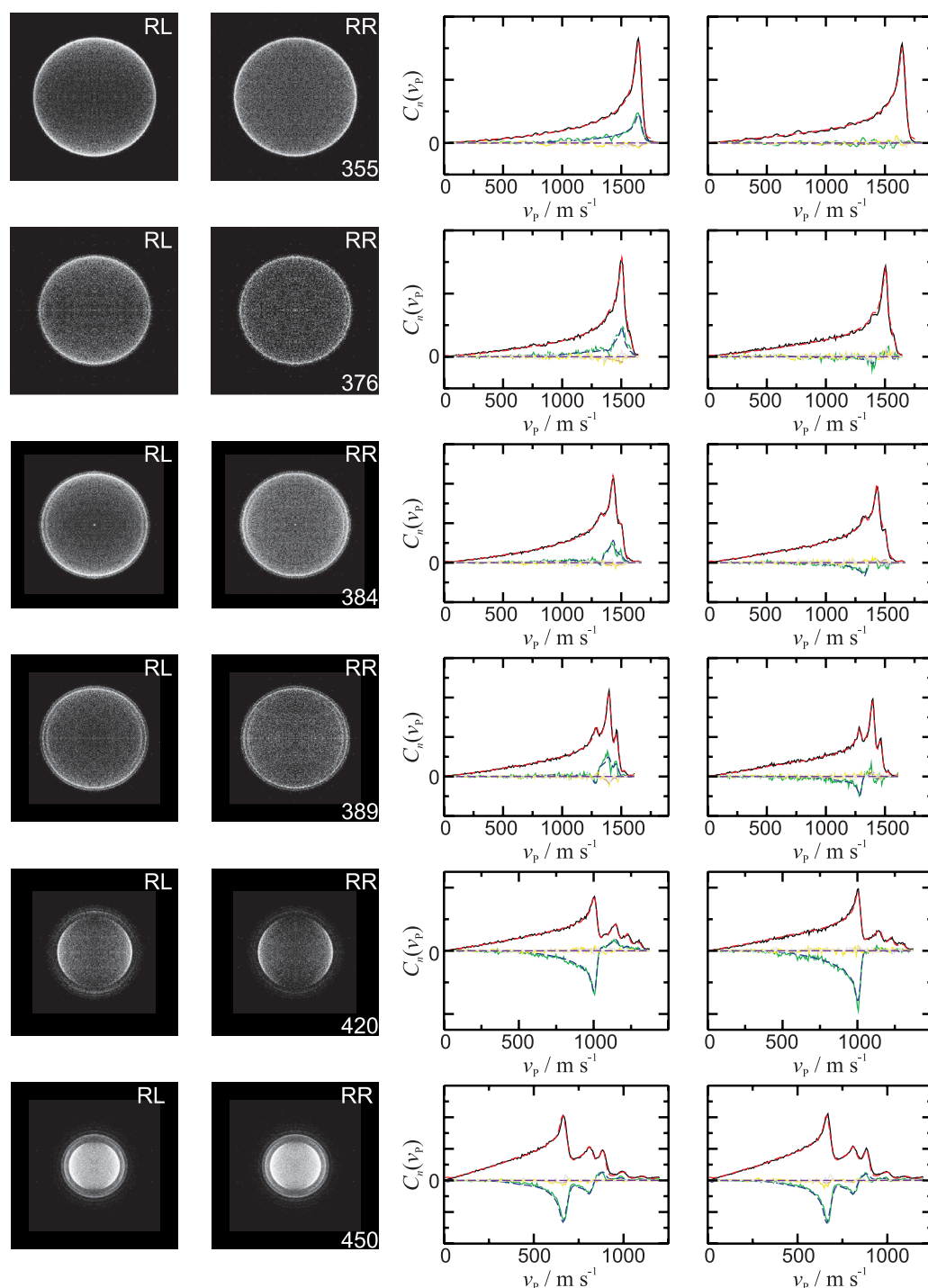


FIG. 2. Ion images for RR and RL circular polarizations of pump and probe lasers, respectively (left), Fourier moments (—) and fits (---) (right) to the CI data, with the $n = 0, 2$, and 4 experimental Fourier moments shown as red, green, and yellow continuous lines. Images recorded using the $^2P_{1/2} \leftarrow ^2P_{3/2}$ REMPI transition at 236.2 nm.

As noted in the accompanying paper,²² the wavepacket calculations shown here and elsewhere in this paper employ constant transition dipole moment functions.^{19,20}

D. Spatial anisotropy parameters

The spatial anisotropy parameter produced by the calculation for the ground state (CI + CI) channel is -1 at every wavelength, as expected for a purely perpendicular excitation.

This is in broad agreement with the experimental data shown in Fig. 6. For the ground state product channel, the new experimental data are consistent with a wavelength independent translational anisotropy, with $\beta = -1$. The near limiting values of β measured here are consistent with a low rotational temperature of the molecular beam, believed to be < 10 K. Previous work at 308 nm has suggested a reduced magnitude of β of -0.88 (not shown in Fig. 6), but this was attributed to rotationally excited parent molecules in the molecular beam.¹²

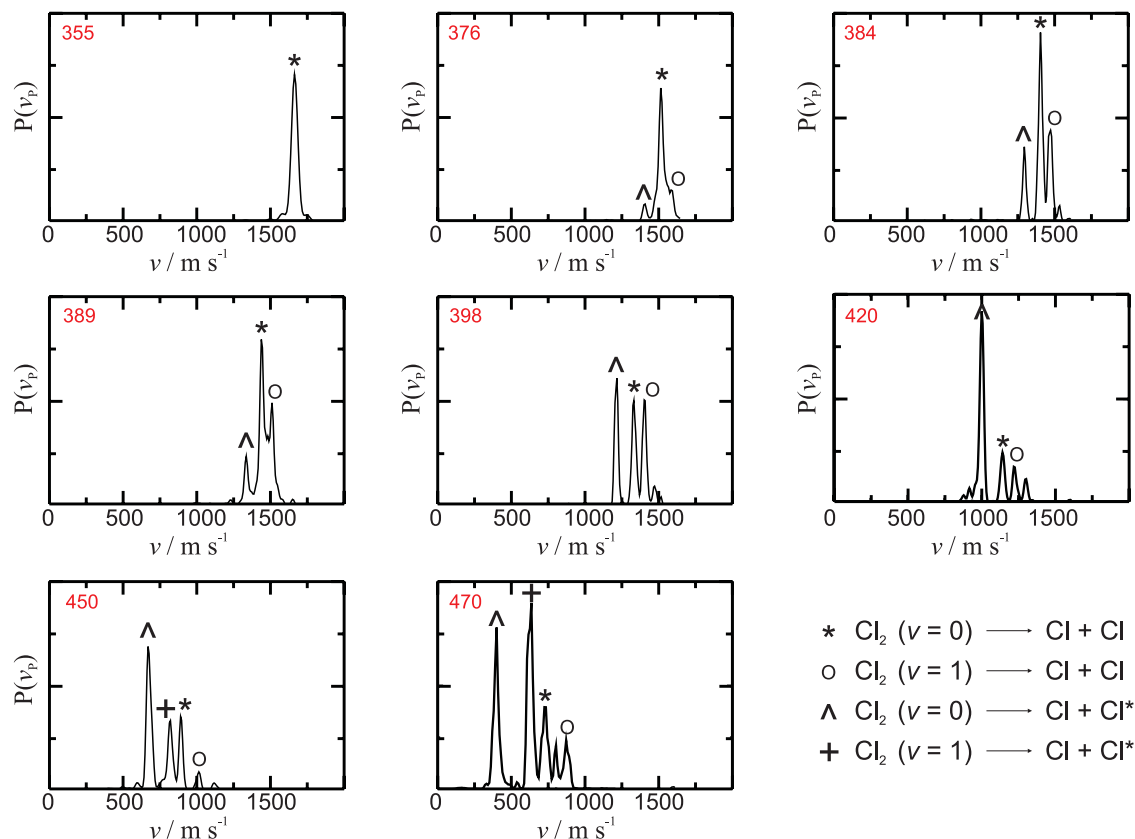
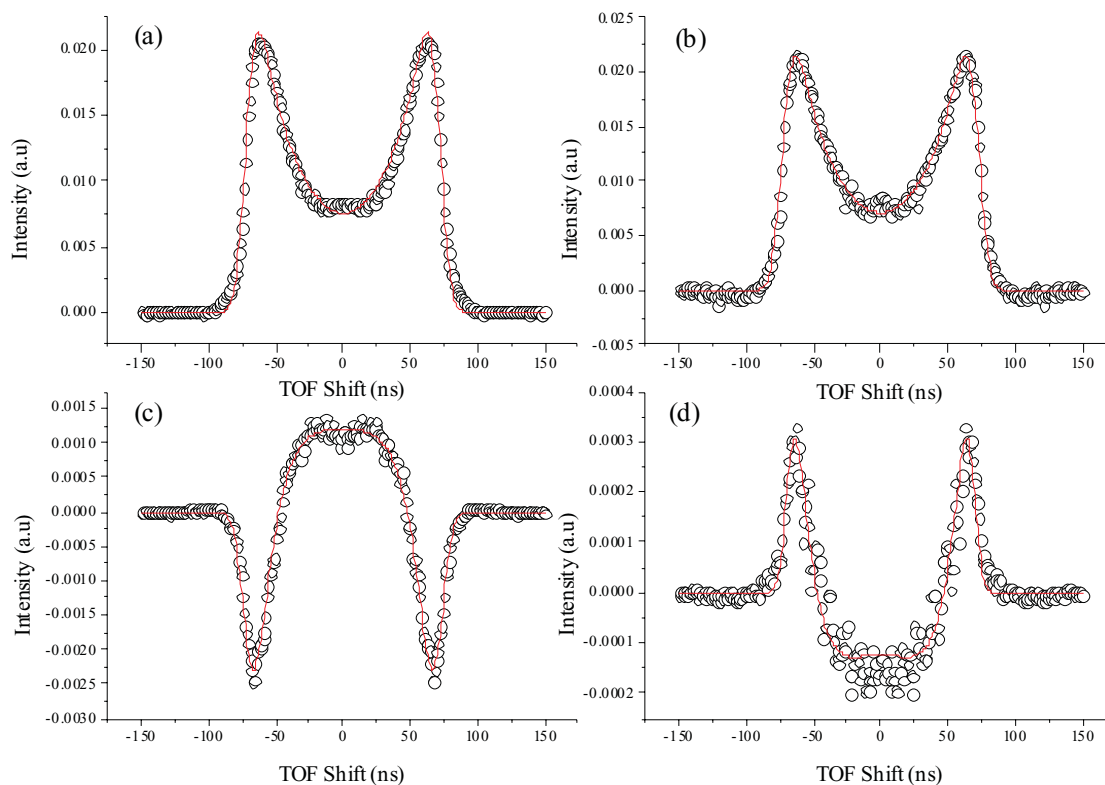
FIG. 3. Speed distributions, $P(v)$, returned from the fits to the Cl Fourier moments at the wavelengths indicated.

FIG. 4. Examples of REMPI TOF data taken at 320 nm and 330 nm. Panels (a) and (b) show symmetrized profiles and simulated fits for the $^{35}\text{Cl}^*$ and $^{37}\text{Cl}^*$ fragments, respectively, for photolysis at 320 nm at the double magic angle geometry; the profiles clearly show the effects of core extraction. Panels (c) and (d) show the effects of vector correlations in determining the shape of the TOF data. Specifically, panel (c) shows the difference profiles and best fit for photolysis at 320 nm using geometry pair I, $\Delta g_I(x)$, while panel (d) shows the difference profile and best fits to the difference profile obtained in geometry pair IV, $\Delta g_{IV}(x)$, for photolysis at 330 nm and detection of $^{35}\text{Cl}^*$.

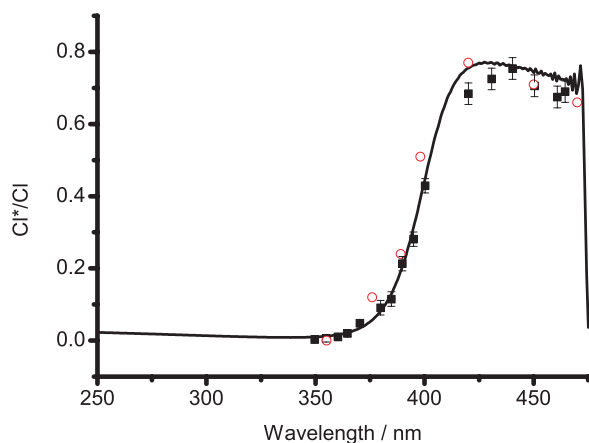


FIG. 5. $\text{Cl}^*(^2\text{P}_{1/2})/\text{Cl}(^2\text{P}_{3/2})$ branching ratio determined from the experimental imaging data (circles) and compared to the theoretical study presented in the accompanying paper (—),²² and with the previous measurements by Samartzis *et al.* (filled squares).¹³ Note that the sharp drop in the branching ratio at 475 nm corresponds to the threshold for making Cl^* .

The spatial anisotropy parameters, β , returned from the fits to both the $\text{Cl}(^2\text{P}_{3/2})$ and $\text{Cl}^*(^2\text{P}_{1/2})$ Fourier moments are also shown in Fig. 6 for dissociation into the excited state product channels. The measured parameters for this channel decrease from a value close to that expected for a pure parallel transition, $\beta = 2$, at long wavelengths to around 1.8 at 355 nm, reflecting the mixed nature of the transition in this region. At wavelengths shorter than 355 nm, the translational anisotropy decreases toward -1 with decreasing wavelength, as the initial excitation step leading to excited state fragments acquires more perpendicular character. At long wavelengths, the dissociation to give excited state products is believed to arise following an adiabatic dissociation on the $\text{B}^3\Pi_{0^+u}$ state potential, resulting in $\beta = 2$. As one moves to shorter wavelengths, however, the excited state channel develops perpendicular character and a sharp reduction in β is seen. For this

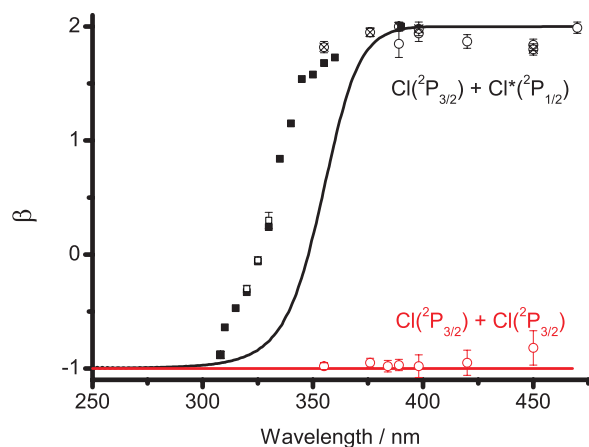


FIG. 6. Spatial anisotropy parameter, β , returned from the fits to the $\text{Cl}(^2\text{P}_{3/2})$ Fourier moments of the ion images (circles) and to the TOF REMPI data (open squares), and compared to the calculated data presented in the accompanying paper (—).²² The data marked with crossed circles are for the excited state channel, but as observed on the $\text{Cl}^*(^2\text{P}_{1/2})$ fragment. Data are shown for dissociation into both the ground (red) and excited (black) state product channels. Previously reported values by Samartzis *et al.*¹³ are represented by solid squares.

channel, the measurements shown in Fig. 6 agree well with those previously made by Samartzis *et al.*¹³ However, there is a discrepancy in wavelength between the experimental values and those calculated from theory.²² This might seem surprising, given that theory seems to reproduce the wavelength dependence of the branching ratio, Cl^*/Cl , very well. However, it should be borne in mind that the Cl^* yield is very low at these wavelengths, where the transition from parallel to perpendicular character occurs.

The discrepancy between the experimental and theoretical wavelength dependence of β for the excited state channel is likely to reflect the relative shape of the calculated $\text{B}^3\Pi_{0^+u}$ state with respect to the other states. In particular, shape of the $\text{B}^3\Pi_{0^+u}$ state relative to the $\text{C}^1\Pi_{1u}$ state will critically effect the form of the β parameter. The position of the curve crossing of the $\text{C}^1\Pi_{1u}$ and the $(1)^3\Sigma_{1u}$ state (see Figs. 1 and 3 of the accompanying paper²²) will also affect this parameter. These aspects of the potentials are liable to be highly sensitive to the details of the *ab initio* calculations, and modeling of the sensitivity of the calculated form of the β parameter to these aspects of the potential energy curves may yield some more insight as to the origins of the current discrepancy between experiment and theory.

Since more than one $\Omega = 1$ state correlates with the excited state channel, measurements of β alone are unable to resolve the precise mechanism for the formation of these products. Likewise, measurements of the translational anisotropy for the ground state product channel, for which $\beta = -1$ across the entire absorption band, are unable to shed light on which of the $\Omega = 1$ symmetry states are involved. Some of these issues are resolved in Subsection III E, which consider the angular momentum polarization of the atom photofragments.

E. Angular momentum polarization

As noted in the accompanying paper, a variety of different formalisms exist to describe the polarization of atoms arising from molecular photodissociation. In the following, we will principally use the laboratory frame polarization parameters of Vasyutinskii and coworkers.^{49–51} However, the link⁵² between these parameters and the commonly used alignment moments of Rakitzis *et al.*^{15,46} are given in Table VII of the accompanying paper.²²

1. Ground state channel, $\text{Cl} + \text{Cl}$

The incoherent alignment parameters s_2 and α_2 returned from the fits to the experimental data are shown in Fig. 7, where they are compared with the theoretical calculations presented in the accompanying paper.²² The theory predicts that $s_2 = 2\alpha_2$ at all dissociation wavelengths, as expected for a purely perpendicular dissociation channel. Both the ion imaging and REMPI TOF experimental data appear to be in good agreement with the theory with respect to both the signs and magnitude of these parameters. Furthermore, the data are in good accord with the previously reported measurements by Brouard and coworkers at 308 nm,¹² Zare and coworkers at 320 nm,¹⁰ and the studies at 355 nm.^{9,11}

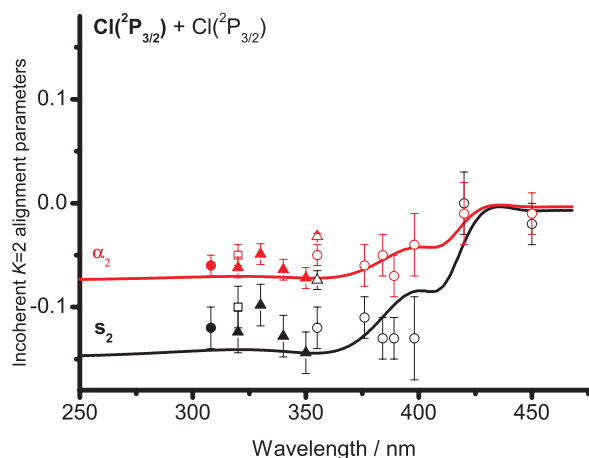


FIG. 7. Incoherent $K = 2$ alignment parameters returned from the fits to the CI Fourier moments of the ion images (open circles) and the TOF REMPI data (solid triangles), and compared to theory (—).²² Data shown for dissociation into the ground state product channel. Previous measurements by Brouard and coworkers at 308 nm (solid circles),¹² Zare and coworkers at 320 nm (open squares),¹⁰ and Bracker *et al.* at 355 nm (open triangles)⁹ are also shown.

At short wavelengths, $\lambda \leq 360$ nm, the values of the incoherent parameters are near limiting. For an adiabatic dissociation process, the incoherent alignment can be predicted by inspection of the expansion coefficients of the molecular wavefunction in the atomic basis at long range.^{49,50,53} These expansion coefficients, in this case computed by consideration of the long range quadrupole-quadrupole interaction, have been given by Alexander.⁵⁴ For the $C^1\Pi_{1u}$ state, the molecular wavefunction can be written as

$$\Psi_{C^1\Pi_{1u}}^{el}(\mathbf{r}, \mathbf{R}) \xrightarrow{R \rightarrow \infty} \left| \frac{3}{2}, \frac{1}{2} \right| \left| \frac{3}{2}, \frac{1}{2} \right\rangle, \quad (17)$$

with the long range expansion coefficient given by

$$T_{\frac{3}{2}, \frac{1}{2}; \frac{3}{2}, \frac{1}{2}}^{C^1\Pi_{1u}} = 1. \quad (18)$$

The expansion coefficients can be used to calculate the asymptotic polarization in the axial recoil limit. For adiabatic dissociation on the $C^1\Pi_{1u}$ state potential, the molecular frame polarization is predicted to be a limiting $a_0^{(2)}(\perp) = -0.8$, which, transformed to the lab frame, gives $s_2 = -0.16$ and $\alpha_2 = -0.08$. In the short wavelength region, $\lambda \leq 360$ nm, theory gives $s_2 = -0.14$ and $\alpha_2 = -0.07$, which is broadly consistent with the picture of *adiabatic* dissociation *via* the $C^1\Pi_{1u}$ state. Following the incoherent excitation of an $\Omega = 1$ or -1 component of the $C^1\Pi_{1u}$ state, adiabatic dissociation on the same sub-state leads to non-zero values of the dynamical function $f_2(1, 1)$, giving rise to the parameters s_2 and α_2 .^{8,9}

The reduction in magnitude of these incoherent parameters even in the short wavelength region, however, indicates the involvement of another state. Inspection of Fig. 8 shows that theory predicts the coherent alignment parameter γ_2 to be zero at all dissociation wavelengths, as expected if there is no parallel component to the channel. The parameter η_2 , however, which is related to the $f_2(1, -1)$ dynamical function, is predicted to be important, even in the short wavelength region. As discussed by Bracker *et al.*, it turns out that this parameter can only arise following a non-adiabatic transition from the

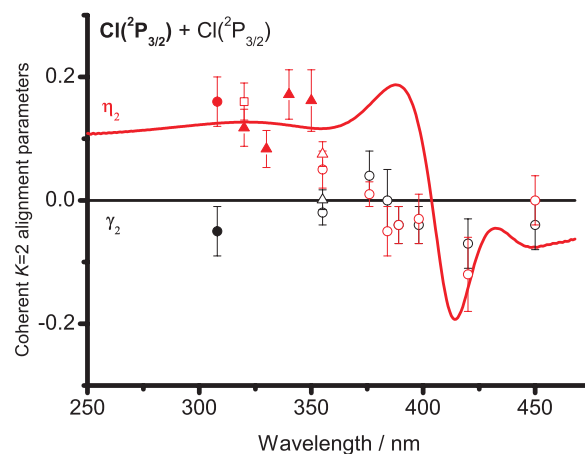


FIG. 8. Coherent $K = 2$ alignment parameters returned from the fits to the CI Fourier moments of the ion images (open circles) and the TOF REMPI data (solid triangles), and compared to the theoretical values (—).²² Data are shown for dissociation into the ground state product channel. Previous measurements by Brouard and co-workers at 308 nm (solid circles),¹² Zare and co-workers at 320 nm (open squares),¹⁰ and Bracker *et al.* at 355 nm (open triangles)⁹ are also shown.

$C^1\Pi_{1u}$ state to the $A^3\Pi_{1u}$ state, which must occur in the long range region of the potentials, where the energy separation between the adiabatic curves is small.^{9,22,55}

There are several possibilities for dissociation following coherent excitation of the $\Omega = \pm 1$ sub-states of the $C^1\Pi_{1u}$ state, both of which are equally populated in the initial excitation step. The molecule may dissociate *via* the same sub-states, *via* a coherent superposition of $A^3\Pi_{1u}$ $\Omega = \pm 1$, or *via* a coherent superposition of the $C^1\Pi_{1u}$ $\Omega = \pm 1$ and $A^3\Pi_{1u}$ $\Omega = \mp 1$ sub-states, with the latter being the only mechanism for production of non-zero η_2 moment.⁹ This mechanism is shown schematically in Fig. 9, with interference between the two pathways (indicated in blue and red) responsible for the variation in η_2 as a function of wavelength. As the dissociation wavelength increases, the magnitudes of the incoherent parameters s_2 and α_2 decrease, which can be taken to mean a rise in the relative importance of the non-adiabatic transition to the $A^3\Pi_{1u}$ state, as outlined above. As discussed by Brouard and coworkers, at longer wavelengths, the optical transition to the $C^1\Pi_{1u}$ state would access less repulsive parts of the potential, resulting in progressively slower timescales associated with the dissociation, facilitating the non-adiabatic transition.¹² The experimental data for the η_2 parameter seem

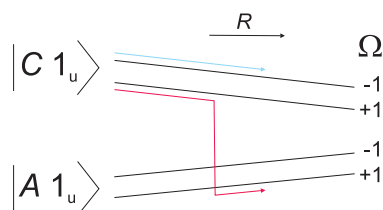


FIG. 9. Only possible mechanism for a non-adiabatic transition leading to non-zero $f_2(1, -1)$. Note that a similar mechanism can be drawn with the non-adiabatic transfer taking place from the $C^1\Pi_{1u}$ $\Omega = -1$ sub-state. This mechanism, however, would be associated with the $f_2(-1, 1)$ dynamical function, which is related to $f_2(1, -1)$ by symmetry.³⁹ Adapted from Ref. 9.

to be in reasonable accord with the quantum calculations,²² particularly the change in sign of the moment as the wavelength is increased (see Fig. 8). In addition, the 355 nm measurements are in good agreement with the previously reported values by Bracker *et al.*⁹ However, the precise details of the wavelength dependence of η_2 are not reproduced exactly by the calculations.

More surprisingly, however, are the experimental measurements of small but non-zero values of the γ_2 parameter, which is related to the $f_2(1, 0)$ dynamical function, at several dissociation wavelengths. A very small but non-zero value of this parameter has previously been reported by Brouard and coworkers following photodissociation at 308 nm.¹² The implications for appearance of the γ_2 parameter are that a parallel transition to an $\Omega = 0$ state is somehow involved in the dissociation mechanism. An $\Omega = 0$ state may be involved in the dissociation either through Coriolis ($\Delta\Omega = \pm 1$) electronic-rotational coupling of the $C^1\Pi_{1u}$ state with an $\Omega = 0$ state or more directly by optical excitation from the ground state. Given that the experimental β parameters are so close to limiting, any parallel component to the excitation process must necessarily be very small. It is interesting to note, however, that consideration of the extremum values of the γ_2 parameter, which for $J = \frac{3}{2}$ are given by⁵²

$$\gamma_2^{\text{extr}} = \pm 0.16 \left[\frac{(1 + \beta)(2 - \beta)}{2} \right]^{1/2}, \quad (19)$$

show that even for a spatial anisotropy parameter β of -0.9 , the magnitude of the parameter γ_2 can be as high as ~ 0.06 . The possible implications of these measurements are discussed in more detail below with regards to the electronic orientation.

Strong orientation has been observed for the ground state product channel, and is clearly visible in the raw ion images recorded using circularly polarized pump and probe radiation, as shown in Fig. 2. Theory predicts that both $K = 1$ and $K = 3$ order orientation moments are important in this channel, however, only the low order, $K = 1$, orientation has been reported previously.¹⁵

The incoherent orientation parameters, α_1 and α_3 , are shown in Fig. 10. α_1 is seen to be wavelength independent, taking a value of ~ 0.13 , with excellent agreement seen between experiment and theory. The value of $\alpha_1 \sim 0.13$ can be understood since incoherent excitation to, and adiabatic dissociation on both of the potentials believed to be important in this channel, $A^3\Pi_{1u}$ and $C^1\Pi_{1u}$, would be expected to give $\alpha_1 = 0.13$ based on long range interactions.⁵⁴ Unfortunately, however, this means that measurements of the α_1 parameter, like those for the spatial anisotropy parameter, are rather insensitive to the non-adiabatic dynamics occurring in this product channel. The parameter α_3 , however, does show some wavelength dependence. In fact, the α_3 parameter shows a similar wavelength dependence to the incoherent alignment parameters s_2 and α_2 . In the case of alignment, the reduction in magnitude of these incoherent parameters as the wavelength increases was taken to be indicative of the importance of non-adiabatic effects. For the incoherent orientation parameter, α_3 , the same reasoning must be applied. The short wave-

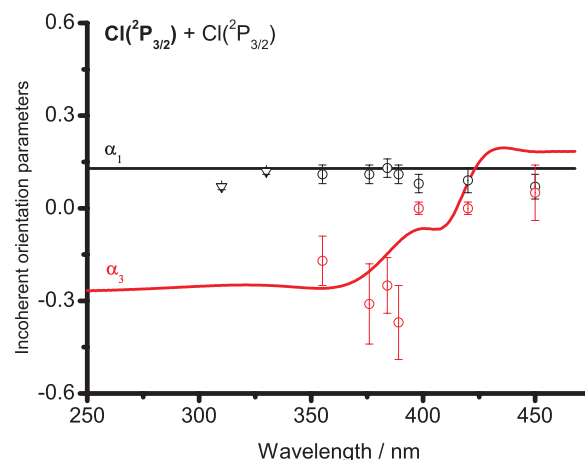


FIG. 10. Incoherent $K = 1$ and 3 orientation parameters returned from the fits to the Cl Fourier moments (open circles) and compared to theory (—).²² Data are shown for dissociation into the ground state product channel. Previous measurements by Zare and coworkers (triangles)¹⁵ are also shown.

length measurements of α_3 seem to be in good agreement with the quantum calculation,²² and the reduction in magnitude with increasing wavelength is also seen experimentally.

The coherent parameter η_3 , related to the $f_3(1, -1)$ dynamical function, is also predicted to be non-zero. Non-zero values of this parameter, like η_2 , indicate interference between the $C^1\Pi_{1u}$ state and $A^1\Pi_{1u}$ state dissociation pathways. As mentioned previously, the non-adiabatic transition between these two states becomes increasingly important in the long wavelength region of the spectrum, which is reflected in the wavelength dependence of η_3 , as shown in Fig. 11. Apart from a slight shift in wavelength of the predicted maximum in η_3 , overall the agreement between experiment and theory is once more satisfactory.

The present theory predicts that the coherent parameters γ_K and γ'_K should be zero since, as discussed previously, the channel is believed to be fully perpendicular in character. The experimental data detailed in Table I, however, indicate non-zero γ'_1 and γ'_3 parameters. As discussed above with

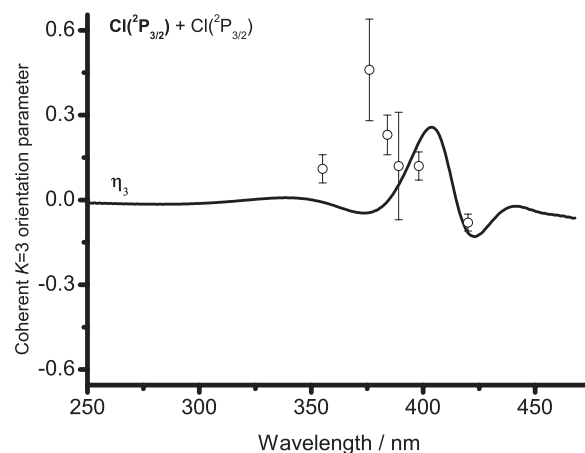


FIG. 11. Coherent η_3 orientation parameter returned from the fits to the Cl Fourier moments (open circles) and compared to the recent theoretical study (—).²² Data are shown for dissociation into the ground state product channel.

TABLE I. Spatial anisotropy and angular momentum polarization parameters for the Cl fragments from the ground state product channel returned from the fits to experimental data. Errors (1σ) in the last digit(s) are given in parenthesis.

Parameter	Wavelength (nm)						
	355	376	384	389	398	420	450
β	-0.98(3)	-0.95(4)	-0.98(5)	-0.97(5)	-0.98(10)	-0.95(11)	-0.82(15)
s_2	-0.12(2)	-0.11(2)	-0.13(2)	-0.13(2)	-0.13(4)	0.00(3)	-0.02(2)
α_2	-0.05(1)	-0.06(2)	-0.05(2)	-0.07(2)	-0.04(3)	-0.01(3)	-0.01(2)
γ_2	-0.02(2)	0.04(4)	0.00(5)	-0.04(3)	-0.04(3)	-0.07(4)	-0.04(4)
η_2	0.05(3)	0.01(2)	-0.05(4)	-0.04(3)	-0.03(4)	-0.12(6)	0.00(4)
α_1	0.11(3)	0.11(3)	0.13(3)	0.11(3)	0.08(3)	0.09(4)	0.07(4)
γ_1	-0.05(3)	-0.07(2)	-0.02(3)	-0.04(1)	-0.02(3)	-0.04(3)	-0.02(5)
γ'_1	-0.04(3)	-0.06(4)	-0.01(3)	0.02(4)	-0.02(4)	0.03(4)	...
α_3	-0.17(8)	-0.31(13)	-0.25(9)	-0.37(12)	0.00(2)	0.00(2)	0.05(9)
γ_3	-0.02(2)	-0.21(16)	-0.25(9)	0.14(26)	0.02(1)	0.12(4)	0.24(30)
γ'_3	0.14(7)	-0.08(17)	0.33(14)	0.26(15)	0.12(5)	0.03(1)	...
η_3	0.11(5)	0.46(18)	0.23(7)	0.12(19)	0.12(5)	-0.08(3)	...

regards to the alignment of the ground state product channel, these coherent parameters indicate the involvement of some $\Omega = 0$ component in the dissociation channel. In particular, there are two mechanisms that could give rise to such coherent parameters:

- Spin-orbit coupling of the ground state to higher triplet *gerade* states allowing a necessarily weak optical transition to take place to the $\Omega = 0$ states correlating with the ground state product channel, see Fig. 2 of Ref. 22.
- Coriolis coupling ($\Delta\Omega = \pm 1$) between one of the *ungerade* $\Omega = 1$ states with the *ungerade* $\Omega = 0$ potential correlating with the ground state channel.

The first such mechanism, in which a spin-forbidden transition takes place to either the $^3\Pi_u(0_u^+)$ or the higher energy $^3\Sigma_u^+(0_u^-)$ state, perhaps weakly allowed *via* spin-orbit coupling between the ground state and triplet states of *gerade* character, is similar to the mechanism which gives rise to the excitation of the $B^3\Pi_{0+u}$ state, important in the excited state product channel. It should be noted that the excited $^3\Pi_u(0_u^+)$ and $^3\Sigma_u^+(0_u^-)$ states, with the second derived from excitation from the $5\sigma_g$ bonding molecular orbital, were not included in the dynamics calculation.²² The absence of these states should not, however, affect the results of the calculations since there are no known electronic transition moments associated with these states.²⁰ The second mechanism, which could give rise to a non-zero parallel component in the dissociation, is coupling of $\Omega = \pm 1$ and $\Omega = 0$ states due to rotation of the nuclear framework, termed Coriolis coupling. It is interesting to note that Coriolis couplings of the $C^1\Pi_{1u}$ and/or $A^3\Pi_{1u}$ states with the $B^3\Pi_{0+u}$ state, important in the excited channel dissociation, were found to be negligible for parent rotational temperatures as high as 300 K.^{5,15}

2. Cl atom from the excited state channel (Cl + Cl*)

The excited state product channel makes a significant contribution to the photodissociation at wavelengths >370 nm, as shown in Fig. 5 and in the accompanying paper.²² In this subsection, we discuss the atomic polarization

arising from this channel, as observed on the ground state Cl photofragment.

At long wavelengths, the theoretical calculation predicts that limiting values are taken by the incoherent alignment parameters, $s_2 = -0.16$ and $\alpha_2 = 0.16$, with zero contributions arising from coherent processes, as shown in Fig. 12. These values, as well as indicating a pure parallel transition (since $s_2 = -\alpha_2$), are predictable based on the long range expansion coefficients assuming that a fully adiabatic dissociation takes place on the $B^3\Pi_{0+u}$ state potential. In the long wavelength region, the experimental results are consistent with this picture, and in good agreement with the previous reported values by Zare and coworkers¹⁰ and Samartzis *et al.*¹³ The latter study (data from which are not shown in Fig. 12) indicated near limiting values of s_2 and α_2 at wavelengths longer than 370 nm.¹³

For wavelengths less than 400 nm, the magnitudes of these incoherent parameters are reduced, indicating that the dissociation can no longer be described as a purely adiabatic process taking place on the $B^3\Pi_{0+u}$ state potential. Zare and coworkers¹⁵ have previously given a mechanism for the

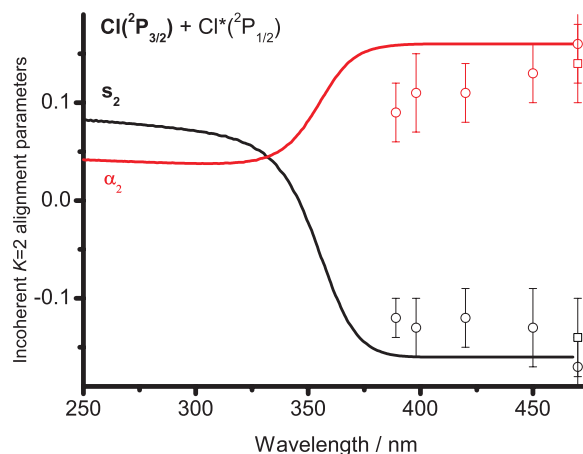


FIG. 12. Incoherent $K = 2$ alignment parameter returned from the fits to the Cl Fourier moments (open circles) and compared to theory (—).²² Data are shown for dissociation into the excited state product channel. Previous measurements by Zare and coworkers (open squares)¹⁰ are also shown.

dissociation into this channel based on electronic orientation measurements of the co-fragment, $\text{Cl}^*(^2\text{P}_{1/2})$ (see the following Subsection III E 3). Their mechanism involves $\text{C}^1\Pi_{1u}$ state excitation followed by a non-adiabatic transition to the $(1)^3\Sigma_{1u}^+$ state, with some additional contribution arising following a further non-adiabatic transition to the $(1)^3\Delta_{1u}$ state.

The molecular wavefunctions in the atomic basis for the three states can be written as

$$\begin{aligned}\Psi_{B^3\Pi_{0+u}}^{el}(\mathbf{r}, \mathbf{R}) &\xrightarrow{R \rightarrow \infty} \frac{1}{2} \left[\left| \frac{3}{2}, \frac{1}{2} \right| \left| \frac{1}{2}, -\frac{1}{2} \right\rangle - \left| \frac{1}{2}, -\frac{1}{2} \right| \left| \frac{3}{2}, \frac{1}{2} \right\rangle \right. \\ &\quad \left. - \left| \frac{3}{2}, -\frac{1}{2} \right| \left| \frac{1}{2}, \frac{1}{2} \right\rangle + \left| \frac{1}{2}, \frac{1}{2} \right| \left| \frac{3}{2}, -\frac{1}{2} \right\rangle \right] \\ \Psi_{(1)^3\Sigma_{1u}^+}^{el}(\mathbf{r}, \mathbf{R}) &\xrightarrow{R \rightarrow \infty} \frac{1}{\sqrt{2}} \left[\left| \frac{3}{2}, \frac{3}{2} \right| \left| \frac{1}{2}, -\frac{1}{2} \right\rangle + \left| \frac{1}{2}, -\frac{1}{2} \right| \left| \frac{3}{2}, \frac{3}{2} \right\rangle \right] \\ \Psi_{(1)^3\Delta_{1u}}(\mathbf{r}, \mathbf{R}) &\xrightarrow{R \rightarrow \infty} \frac{1}{\sqrt{2}} \left[\left| \frac{3}{2}, \frac{1}{2} \right| \left| \frac{1}{2}, \frac{1}{2} \right\rangle + \left| \frac{1}{2}, \frac{1}{2} \right| \left| \frac{3}{2}, \frac{1}{2} \right\rangle \right]. \quad (20)\end{aligned}$$

Inspection of the long range coefficients enables prediction of the atomic alignment, $a_0^{(2)}$, based on adiabatic dissociation on each of the above states. For the $B^3\Pi_{0+u}$ state, $a_0^{(2)} = -0.8$, giving $s_2 = -0.16$ and $\alpha_2 = 0.16$ in the lab frame, as mentioned above. For the $(1)^3\Sigma_{1u}^+$ state, $a_0^{(2)} = 0.8$, giving $s_2 = 0.16$ and $\alpha_2 = 0.08$, while for the $(1)^3\Delta_{1u}$ state, $a_0^{(2)} = -0.8$. This value is the same as for the $B^3\Pi_{0+u}$ state, however, in this case, $s_2 = -0.16$ and $\alpha_2 = -0.08$ since this state would be associated with a perpendicular rather than parallel transition.

The experimental results show a decrease in the magnitude of the parameters for wavelengths < 400 nm, as mentioned above. The trends in the experimental data are therefore consistent, based on the above adiabatic polarization arguments, with the picture of non-adiabatic transfer from the $\text{C}^1\Pi_{1u}$ to $(1)^3\Sigma_{1u}^+$ state as being the dominant mechanism for production of the excited state product channel in the short wavelength region. This picture is confirmed by the theoretical work presented here and in the accompanying paper.²²

The coherent parameters γ_2 and η_2 are also predicted to be important in the short wavelength region, as shown in Fig. 13. The non-zero values taken by the parameter γ_2 , which is related to the $f_2(1, 0)$ dynamical function, are consistent with an interference between the $B^3\Pi_{0+u}$ and $(1)^3\Sigma_{1u}^+/(1)^3\Delta_{1u}$ state dissociation pathways. The manifestation of η_2 , on the other hand, is consistent with interference between the $(1)^3\Sigma_{1u}^+$ and $(1)^3\Delta_{1u}$ states. The present study is the first to observe coherent alignment effects for this dissociation channel. The experimental measurements of the electronic alignment for this channel are in qualitative accord with the theoretical calculation and support the mechanism given by Zare and coworkers.¹⁵

The incoherent orientation parameters α_1 and α_3 for the excited state product channel are shown in Fig. 14 along with theoretical values for comparison. At long wavelengths, > 400 nm, there is no orientation. In this region, as discussed above with respect to the electronic alignment of Cl in this channel, the dissociation can be viewed as proceeding adiabatically on the $B^3\Pi_{0+u}$ state potential. The long wavelength behaviour of α_1 and α_3 therefore follows, since a pure parallel

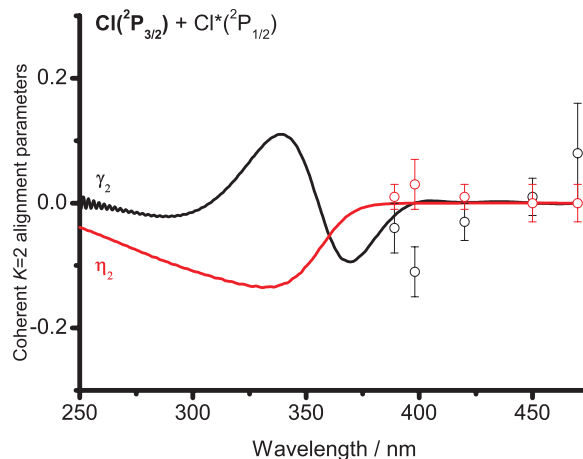


FIG. 13. Coherent $K = 2$ alignment parameter returned from the fits to the Cl Fourier moments (open circles) and compared to theory (—).²² Data are shown for dissociation into the excited state product channel.

transition results in zero orientation within the framework of the axial recoil approximation.³⁹

Moving to shorter wavelengths, both α_1 and α_3 are seen to take non-zero values, with theory predicting a positive α_1 and a small, negative α_3 . In this region, the spatial anisotropy parameter, β , decreases indicating that a perpendicular state is involved in the dissociation. The positive value of $\alpha_1 \sim 0.3$ reached at ~ 330 nm implies a molecular frame orientation of $a_0^{(1)}(\perp) \sim 0.6$. By inspection of the long range expansion coefficients, the dominant $\Omega = 1$ contribution to the dissociation channel must therefore come from the $(1)^3\Sigma_{1u}^+$ state, which is in agreement with the findings of Zare and coworkers¹⁵ and Asano and Yabushita,¹⁷ and with the above discussion regarding the electronic alignment for this dissociation channel. The value predicted by theory, $a_0^{(1)}(\perp) \sim 0.6$, is somewhat less than the limiting $a_0^{(1)}(\perp) = 0.78$ expected for adiabatic dissociation on the $(1)^3\Sigma_{1u}^+$ state potential.⁵⁴ Since in this short wavelength region, the spatial anisotropy parameter, $\beta = -1$, another $\Omega = 1$ state must make a contribution to the dissociation. The only other $\Omega = 1$ state correlating with this

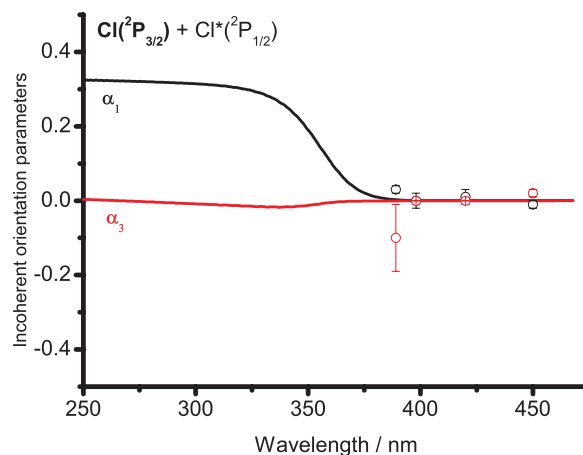


FIG. 14. Incoherent $K = 1$ and 3 orientation parameters returned from the fits to the Cl Fourier moments (open circles) and compared to theory (—).²² Data are shown for dissociation into the excited state product channel.

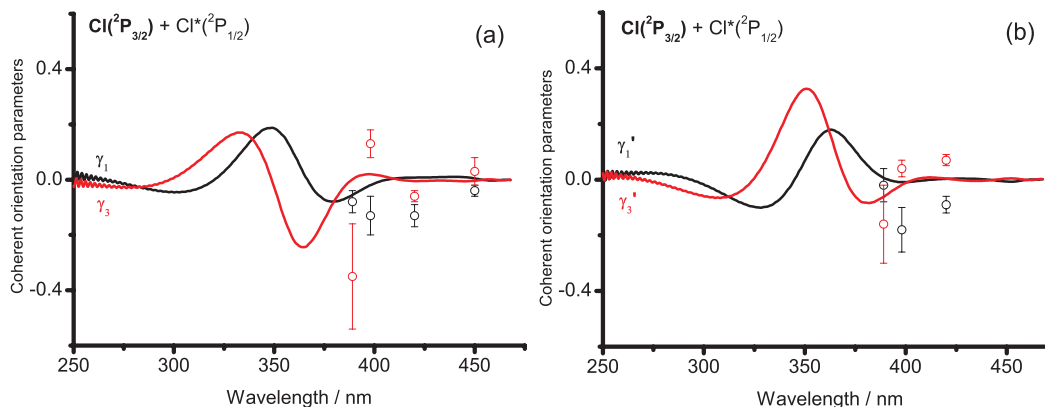


FIG. 15. Coherent $K = 1$ and 3 orientation parameters returned from the fits to the Cl Fourier moments (open circles) and compared to the recent theoretical study (—).²² The parameters γ_1 and γ_3 are shown in (a), while γ'_1 and γ'_3 are shown in (b). Data are shown for dissociation into the excited state product channel.

dissociation channel is the $(1)^3\Delta_{1u}$ state, which, in the adiabatic limit, gives a much smaller $a_0^{(1)}(\perp)$ of 0.26. The incoherent orientation parameters are therefore consistent with an additional non-adiabatic transition to the $(1)^3\Delta_{1u}$ state, as first described by Zare and coworkers.¹⁵

For this excited dissociation channel, as opposed to the ground state channel, coherent orientation parameters are predicted to arise as a result of interference between parallel, $\Delta\Omega = 0$, and perpendicular, $\Delta\Omega = \pm 1$, dissociation pathways. Non-zero values for γ_K and γ'_K ($K = 1, 3$) are found at shorter wavelengths, as shown in Fig. 15, where the β parameter decreases from its limiting value of 2. At the wavelengths studied here, the orientation of the Cl fragment only just begins to be important. Nevertheless, non-zero values of the coherent orientation parameters are seen, for the first time, in the shorter wavelength measurements.

The spatial anisotropy parameters, β , and angular momentum alignment and orientation parameters for dissociation to both the ground and excited state product channels reported following measurements of the Cl fragment are summarized in Tables I and II.

TABLE II. Spatial anisotropy and angular momentum polarization parameters for the Cl fragments partnered by Cl^* in the excited state product channel returned from the fits to experimental data. Errors (1σ) in the last digit(s) are given in parenthesis.

Parameter	Wavelength (nm)				
	389	398	420	450	470
β	1.85(12)	1.94(7)	1.87(6)	1.84(5)	1.99(5)
s_2	-0.12(2)	-0.13(3)	-0.12(3)	-0.13(4)	-0.17(3)
α_2	0.09(3)	0.11(4)	0.11(3)	0.13(3)	0.16(4)
γ_2	-0.04(4)	-0.11(4)	-0.03(3)	0.01(3)	0.08(8)
η_2	0.01(2)	0.03(4)	0.01(2)	0.00(3)	0.00(3)
α_1	0.03(1)	-0.00(2)	0.01(2)	-0.01(1)	...
γ_1	-0.08(4)	-0.13(7)	-0.13(4)	-0.04(2)	...
γ'_1	-0.02(6)	-0.18(8)	-0.09(3)
α_3	-0.10(9)	0.00(0)	-0.00(0)	0.02(1)	...
γ_3	-0.35(23)	0.13(5)	-0.06(2)	0.03(5)	...
γ'_3	-0.16(14)	0.04(3)	0.07(2)
η_3	-0.35(22)	0.19(19)	0.01(1)

3. Cl^* atom from the excited state channel, ($\text{Cl}^* + \text{Cl}$)

In this subsection, we discuss the atomic orientation arising from this channel, as observed on the excited state Cl^* photofragment. At long wavelengths, only the spatial anisotropy parameter was determined since in this region the excited state channel predominantly arises following adiabatic dissociation on the $B^3\Pi_{0+u}$ state potential. For a purely parallel transition, no orientation of the electronic angular momentum is possible, and since $J = \frac{1}{2}$ for this fragment, there cannot be alignment. At shorter wavelengths, however, low order orientation was observed, both in the ion imaging and the TOF REMPI studies. These are shown in Fig. 16, where they are compared to the theoretical calculations²² and to the previous experimental results from Zare and coworkers¹⁴ for both the $^{35}\text{Cl}^*$ and $^{37}\text{Cl}^*$ photofragments.

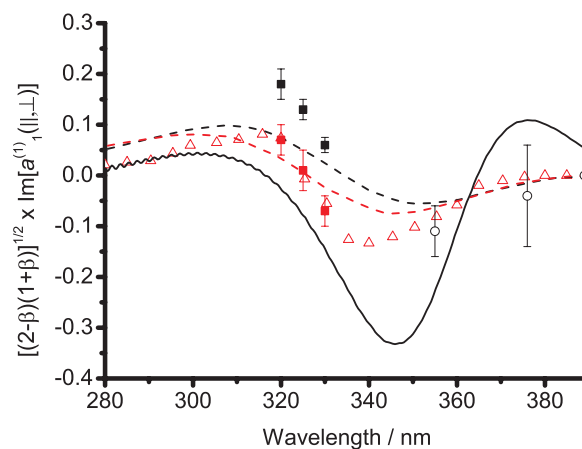


FIG. 16. $\text{Im}[a_1^{(1)}(||, \perp)]$ parameter, multiplied by the factor $[(2 - \beta)(1 + \beta)]^{1/2}$ for the Cl^* fragments in the $\text{Cl} + \text{Cl}^*$ product channel. The solid black line represents the theoretical work described in the accompanying paper.²² The experimental data returned from fits to the Fourier moments of the ion images are represented by open circles, while the TOF REMPI data are shown as filled squares. Also shown is the $\text{Im}[a_1^{(1)}(||, \perp)]$ parameter reported from the theoretical work by Asano and Yabushita¹⁷ for $^{35}\text{Cl}^*$ (black dashed) and $^{37}\text{Cl}^*$ (red dashed) fragments. Previous measurements by Zare and coworkers¹⁴ are represented by open triangles for $^{35}\text{Cl}^*$ (black) and $^{37}\text{Cl}^*$ (red). Note that the sign of the theoretical data has been inverted.

TABLE III. Spatial anisotropy and angular momentum polarization parameters for the Cl* fragments from the excited state product channel returned from the fits to experimental data. Errors (1σ) in the last digit(s) are given in parenthesis.

Parameter	Wavelength (nm)							
	320	325	330	355	376	389	398	450
β	-0.30(7)	-0.05(7)	0.30(14)	1.82(5)	1.95(4)	2.00(4)	1.98(6)	1.80(5)
α_1	-0.02(2)	-0.00(2)
γ_1	-0.21(16)	-0.07(7)
γ'_1	-0.15(6)	-0.12(4)	-0.06(3)	0.05(4)	0.01(4)

Consistent with previous work, the γ'_1 parameter is found to be non-zero for the Cl* fragment. This parameter arises following quantum mechanical interference between the $B^3\Pi_{0+u}$ and $(1)^3\Sigma_{1u}^+$ state pathways giving rise to the excited state product channel. Using the definitions given in the accompanying paper,²² γ'_1 is proportional to the molecular frame parameter $\text{Im}[a_1^{(1)}(\parallel, \perp)]$ multiplied by the factor $[(2 - \beta)(1 + \beta)]^{1/2}$. This molecular frame parameter has been modeled theoretically by Asano and Yabushita¹⁷ using the Young's double slit method to estimate the phase difference, $\Delta\phi$, between the parallel transition to the $B^3\Pi_{0+u}$ state and the perpendicular transition to the $(1)^3\Sigma_{1u}^+$ state, and their subsequent dissociation dynamics. Using the model, the $\text{Im}[a_1^{(1)}(\parallel, \perp)]$ parameter could be expressed as¹⁷

$$\text{Im}[a_1^{(1)}(\parallel, \perp)] \propto \sqrt{(1 + \beta) \left(1 - \frac{\beta}{2}\right)} \sin(\Delta\phi). \quad (21)$$

The $\text{Im}[a_1^{(1)}(\parallel, \perp)]$ parameter for the $^{35}\text{Cl}^*$ and $^{37}\text{Cl}^*$ fragments, as calculated by Asano and Yabushita¹⁷ using Eq. (21), is also shown in Fig. 16. The $\text{Im}[a_1^{(1)}(\parallel, \perp)]$ parameter calculated by Asano and Yabushita¹⁷ is in qualitative agreement with all of the available experimental data, correctly predicting the phase shift due to the different de Broglie wavelengths associated with the $^{35}\text{Cl}^*$ and $^{37}\text{Cl}^*$ fragments. Results from the theoretical calculation²² show the same oscillatory structure, but there is a sign difference between the calculations and the experimental results observed here and those previously reported values by Zare and coworkers,¹⁴ the origin of which is unclear. Table III summarizes the spatial anisotropy and angular momentum orientation parameters returned from the fits to the experimental data (obtained by both ion imaging and REMPI TOF) for the Cl* fragments.

Unlike the orientation parameters, α_K and γ_K , which may arise following photodissociation using circularly polarized light and result from the helicity of the dissociation photon, the orientation parameter γ'_1 , and therefore $\text{Im}[a_1^{(1)}(\parallel, \perp)]$, is produced following photodissociation using linearly polarized light and is related to the alignment of the photolysis photon.⁵² Using a classical description of two orthogonal oscillations, Zare and coworkers provided an instructive discussion on the manifestation of such electronic orientation following photolysis using linearly polarized light.¹⁰ When parallel and perpendicular transitions are excited coherently at a particular photon energy, a phase difference arises due to the different speeds at which the wavepackets progress along the potential energy curves of the two different electronic states. If circularly polarized light is used, this phase

difference gives rise to a helicity in the electronic charge distribution.¹⁴ Measurements of such helicity, and therefore phase difference, provide a very sensitive test of the potentials sampled on route to dissociation.

IV. CONCLUSIONS AND FUTURE WORK

The photodissociation of molecular chlorine has been investigated at a range of energies, from close to 300 nm, out to the long wavelength region, 470 nm. Experimentally, the velocity map ion imaging and REMPI TOF techniques have been used to probe the velocity and angular momentum distributions of the resulting atomic fragments. The experimental results presented here have been compared with quantum mechanical time dependent wavepacket calculations, performed on a set of high level *ab initio* potentials,²⁰ and are presented in more detail in the accompanying paper.²² The calculations provide the first prediction of all angular momentum polarization information amenable to the Cl_2 system. From this detailed study, high order, $K = 3$, polarization was predicted to be important for the Cl photofragments. The current work provides the first experimental measurements of such orientation moments. In general, good agreement was found between current experiment and theory, as well as with the previous experimental measurements. Any discrepancies between theory and experiment are discussed below in the context of possible future work.

The data presented here are in excellent agreement with previous work, and generally support the previously made assertions regarding the subtle mechanisms by which the Cl_2 molecule dissociates. The Cl + Cl product channel dominates the short wavelength region with excitation to, and adiabatic dissociation on, the $C^1\Pi_{1u}$ state potential giving rise to the majority of the products. As the wavelength increases, a significant non-adiabatic transition from the $C^1\Pi_{1u}$ to $A^3\Pi_{1u}$ state takes place, with the effects of this encoded in both the experimental and theoretical polarization parameters. At the other end of the absorption spectrum, the Cl + Cl* channel dominates with excitation to, and adiabatic dissociation occurring on, the $B^3\Pi_{0+u}$ state potential. At shorter wavelengths, perpendicular components to the dissociation channel become important. In particular, a non-adiabatic transition from the $C^1\Pi_{1u}$ to $(1)^3\Sigma_{1u}^+$ state takes place and results in the Cl + Cl* developing purely perpendicular character. Moreover, an additional transition takes place to the $(1)^3\Delta_{1u}$ state giving rise to coherent polarization resulting from two perpendicular electronic transitions. Where the $B^3\Pi_{0+u}$, $(1)^3\Sigma_{1u}^+$,

and $(1)^3\Delta_{1u}$ state dissociation pathways overlap, significant interference effects result.

The results presented here point to several possibilities regarding future experimental and theoretical work. Although in good general agreement with theory, the experimental polarization data for dissociation into the ground state product channel carry the fingerprints of a parallel transition to an $\Omega = 0$ state. No such state has previously been discussed, and could only arise through two mechanisms; either a direct excitation could take place to one of the two $\Omega = 0$ states correlating with the product channel or a Coriolis type coupling, $\Delta\Omega = \pm 1$, could give rise to population in one of these states as the dissociation proceeds. The second mechanism could be investigated relatively easily by monitoring the dissociation as a function of the rotational temperature of the molecular beam.

Another slight discrepancy with theory was found at 450 nm, where the measured spatial anisotropy seems to be somewhat smaller than the limiting values predicted by theory. The observed discrepancies are larger than might be expected for non-axial recoil behaviour, given the rather low rotational temperature of the parent molecule, estimated to be around 10 K in the relevant experiments. This suggests that the deviations in the measured spatial anisotropy from the limiting values reflect the underlying dissociation dynamics, implying that adiabatic dissociation on the $B^3\Pi_{0+u}$ state potential in this wavelength region is not the only dissociation pathway. A disagreement between experiment and theory was also found regarding the position at which the spatial anisotropy parameter, β , starts to decrease from its limiting value of +2 in the excited state product channel. While the theory appears to predict correctly both the Cl^*/Cl branching ratio and the shape of the experimentally observed decrease in β , the wavelength at which this takes place is shifted somewhat. Further electronic structure studies would therefore be useful in order to understand this effect.

Finally, the ion imaging experiments also potentially yield information of the photodissociation dynamics of Cl_2 initially excited in $v = 1$. These molecules are only inefficiently cooled in the molecular beam expansion. A forthcoming paper⁴⁸ will present a detailed comparison between experiment and theory for this vibrationally excited dissociation process.

ACKNOWLEDGMENTS

The support of the Engineering and Physical Sciences Research Council, U.K., (to M.B. and G.A.D.R. *via* Programme Grant No. EP/G00224X1), the European Union (to M.B. *via* FP7 EU People ITN project 238671), and the Deutsche Forschungsgemeinschaft (to R.J.B. *via* Grant No. BU 450/21-2). AB thanks the Natural Sciences Engineering Research Council of Canada (Discovery Grant) for financial support.

¹G. E. Busch, R. T. Mahoney, R. I. Morse, and K. R. Wilson, *J. Chem. Phys.* **51**, 449 (1969).

²R. W. Diesen, J. C. Wahr, and S. E. Adler, *J. Chem. Phys.* **50**, 5635 (1969).

³L. Li, R. J. Lipert, J. Lobue, W. A. Chupka, and S. D. Colson, *Chem. Phys. Lett.* **151**, 335 (1988).

⁴Y. Matsumi, M. Kawasaki, T. Sato, T. Kinugawa, and T. Arikawa, *Chem. Phys. Lett.* **155**, 486 (1989).

⁵Y. Matsumi, K. Tonokura, and M. Kawasaki, *J. Chem. Phys.* **97**, 1065 (1992).

⁶P. C. Samartzis, I. Sakellariou, T. Gougousi, and T. N. Kitsopoulos, *J. Chem. Phys.* **107**, 43 (1997).

⁷Y. Wang, H.-P. Looock, J. Cao, and C. X. W. Qian, *J. Chem. Phys.* **102**, 808 (1995).

⁸A. S. Bracker, E. R. Wouters, A. G. Suits, Y. T. Lee, and O. S. Vasyutinskii, *Phys. Rev. Lett.* **80**, 1626 (1998).

⁹A. S. Bracker, E. R. Wouters, A. G. Suits, and O. S. Vasyutinskii, *J. Chem. Phys.* **110**, 6749 (1999).

¹⁰T. P. Rakitzis, S. A. Kandel, A. J. Alexander, Z. H. Kim, and R. N. Zare, *J. Chem. Phys.* **110**, 3351 (1999).

¹¹T. P. Rakitzis and T. N. Kitsopoulos, *J. Chem. Phys.* **116**, 9228 (2002).

¹²M. J. Bass, M. Brouard, A. P. Clark, B. Martínez-Haya, and C. Vallance, *Phys. Chem. Chem. Phys.* **5**, 856 (2003).

¹³P. C. Samartzis, B. L. G. Bakker, T. P. Rakitzis, D. H. Parker, and T. N. Kitsopoulos, *J. Chem. Phys.* **110**, 5201 (1999).

¹⁴Z. H. Kim, A. J. Alexander, S. A. Kandel, T. P. Rakitzis, and R. N. Zare, *Faraday Discuss.* **113**, 27 (1999).

¹⁵A. J. Alexander, Z. H. Kim, S. A. Kandel, R. N. Zare, T. P. Rakitzis, Y. Asano, and S. Yabushita, *J. Chem. Phys.* **113**, 9022 (2000).

¹⁶S. D. Peyerimhoff and R. J. Buenker, *Chem. Phys.* **57**, 279 (1981).

¹⁷Y. Asano and S. Yabushita, *J. Phys. Chem. A* **105**, 9873 (2001).

¹⁸Y. Asano and S. Yabushita, *Chem. Phys. Lett.* **372**, 348 (2003).

¹⁹D. B. Kokh, A. B. Alekseyev, and R. J. Buenker, *J. Chem. Phys.* **115**, 9298 (2001).

²⁰D. B. Kokh, A. B. Alekseyev, and R. J. Buenker, *J. Chem. Phys.* **120**, 11549 (2004).

²¹L. G. M. de Macedo and W. A. de Jong, *J. Chem. Phys.* **128**, 041101 (2008).

²²A. J. Johnsen, A. B. Alekseyev, G. G. Balint-Kurti, M. Brouard, A. Brown, R. J. Buenker, E. K. Campbell, and D. B. Kokh, *J. Chem. Phys.* **136**, 164310 (2012).

²³P. M. Regan, D. Ascenzi, A. Brown, G. G. Balint-Kurti, and A. J. Orr-Ewing, *J. Chem. Phys.* **112**, 10259 (2000).

²⁴A. Brown and G. G. Balint-Kurti, *J. Chem. Phys.* **113**, 1870 (2000).

²⁵G. G. Balint-Kurti, A. J. Orr-Ewing, J. A. Beswick, A. Brown, and O. S. Vasyutinskii, *J. Chem. Phys.* **116**, 10760 (2002).

²⁶A. Brown, G. G. Balint-Kurti, and O. S. Vasyutinskii, *J. Phys. Chem. A* **108**, 7790 (2004).

²⁷A. G. Smolin, O. S. Vasyutinskii, G. G. Balint-Kurti, and A. Brown, *J. Phys. Chem. A* **110**, 5371 (2006).

²⁸A. T. J. B. Eppink and D. H. Parker, *Rev. Sci. Instrum.* **68**, 3477 (1997).

²⁹D. W. Chandler and P. L. Houston, *J. Chem. Phys.* **87**, 1 (1987).

³⁰M. Brouard, R. Cireasa, A. P. Clark, G. C. Groenenboom, G. Hancock, S. Horrocks, F. Quadrini, G. A. D. Ritchie, and C. Vallance, *J. Chem. Phys.* **125**, 133308 (2006).

³¹M. Bass, M. Brouard, A. P. Clark, and C. Vallance, *J. Chem. Phys.* **117**, 8723 (2002).

³²M. Brouard, R. Cireasa, A. P. Clark, F. Quadrini, and C. Vallance, *Phys. Chem. Chem. Phys.* **8**, 5549 (2006).

³³M. Brouard, A. V. Green, F. Quadrini, and C. Vallance, *J. Chem. Phys.* **127**, 084304 (2007).

³⁴M. Brouard, F. Quadrini, and C. Vallance, *J. Chem. Phys.* **127**, 084305 (2007).

³⁵S. K. Lee, D. Townsend, O. S. Vasyutinskii, and A. G. Suits, *Phys. Chem. Chem. Phys.* **7**, 1650 (2005).

³⁶M. Ahmed, D. S. Peterka, A. S. Bracker, O. S. Vasyutinskii, and A. G. Suits, *J. Chem. Phys.* **110**, 4115 (1999).

³⁷A. G. Smolin, O. S. Vasyutinskii, E. R. Wouters, and A. G. Suits, *J. Chem. Phys.* **121**, 6759 (2004).

³⁸Y. Mo and T. Suzuki, *J. Chem. Phys.* **109**, 4691 (1998).

³⁹L. D. A. Siebbeles, M. Glass-Maujean, O. S. Vasyutinskii, J. A. Beswick, and O. Roncero, *J. Chem. Phys.* **100**, 71913610 (1994).

⁴⁰R. N. Zare, *Angular Momentum, Understanding Spatial Aspects in Chemistry and Physics* (Wiley, New York, 1988).

⁴¹G. Hancock, P. J. Pearson, G. A. D. Ritchie, and D. F. Tibbetts, *Phys. Chem. Chem. Phys.* **5**, 5386 (2003).

⁴²S. Arapelli, N. Presser, D. Robie, and R. Gordon, *Chem. Phys. Lett.* **118**, 88 (1985).

⁴³M. Mons and I. Dimicoli, *J. Chem. Phys.* **90**, 4037 (1989).

⁴⁴R. N. Dixon, *J. Chem. Phys.* **85**, 1866 (1986).

- ⁴⁵MATLAB, Version 7.9.0.559 (R2009b).
- ⁴⁶T. P. Rakitzis and R. N. Zare, *J. Chem. Phys.* **110**, 3341 (1999).
- ⁴⁷T. P. Rakitzis, G. E. Hall, M. L. Costen, and R. N. Zare, *J. Chem. Phys.* **111**, 8751 (1999).
- ⁴⁸E. K. Campbell, A. B. Alekseyev, M. Brouard, G. G. Balint-Kurti, A. Brown, R. J. Buenker, R. Cireasa, A. J. Johnsen, D. B. Kokh, S. Lucas, and B. Winter, "The vibrationally mediated photodissociation of Cl₂" (unpublished).
- ⁴⁹O. S. Vasyutinskii, *Sov. Phys. JETP* **54**, 855 (1981).
- ⁵⁰O. S. Vasyutinskii, *Opt. Spectrosc.* **54**, 524 (1983).
- ⁵¹B. V. Picheyev, A. G. Smolin, and O. S. Vasyutinskii, *J. Phys. Chem. A* **101**, 7614 (1997).
- ⁵²A. G. Suits and O. S. Vasyutinskii, *Chem. Rev.* **108**, 3706 (2008).
- ⁵³J. A. Beswick and O. S. Vasyutinskii, *Comments At. Mol. Phys.* **42**, 69 (1998).
- ⁵⁴A. J. Alexander, *Phys. Chem. Chem. Phys.* **7**, 3693 (2005).
- ⁵⁵E. R. Wouters, M. Ahmed, D. S. Peterka, A. S. Bracker, A. G. Suits, and O. S. Vasyutinskii, in *Imaging in Chemical Dynamics*, edited by A. G. Suits and R. E. Continetti (American Chemical Society, Washington, DC, 2000), Chap. 15, pp. 238–284.